International Journal of Chemistry, Mathematics and Physics (IJCMP)
[Vol-10, Issue-3, July-September, 2026]
https://dx.doi.org/10.22161/ijcmp.10.3.1
ISSN: 2456-866X

Mathematical Modelling and Multi-Objective Optimization of an Inerter-Based Dynamic Vibration Absorber

Sultan Mahamdnur Ibrahim

Faculty of Mechanical and Industrial Engineering, Aksum University, Aksum, Ethiopia
Email: sultanmahamad16@gmail.com or sultan.m.ibrahim@mail.aku.edu.et

Received: 30 May 2026; Received in revised form: 28 June 2026; Accepted: 01 July 2026; Available online: 08 July 2026

Abstract— *This study presents the mathematical modelling and multi-objective optimization of a passive inerter-based dynamic vibration absorber for suppressing vibration in a lightly damped primary structure. A two-degree-of-freedom model is formulated in which a grounded inerter augments the apparent inertia of the absorber without introducing an equivalent increase in physical mass. Analytical frequency-response functions and a state-space representation are derived to evaluate both steady-state and transient behaviour. The absorber tuning ratio, damping ratio, and inertance ratio are optimized using the Non-dominated Sorting Genetic Algorithm II (NSGA-II). Two competing objectives are considered: minimization of the worst-case primary-mass displacement transmissibility and minimization of the normalized absorber stroke. The resulting Pareto front is used to identify a balanced compromise design through knee-point, equal-weight, and minimum-distance-to-utopia criteria. For the selected design, the optimized tuning, damping, and inertance ratios are 1.50, 0.465, and 0.108, respectively. The inerter increases the apparent absorber inertia to approximately 3.2 times its physical mass. Compared with the uncontrolled structure, the optimized inerter-based absorber reduces the peak transmissibility from 25.0 to 3.45, corresponding to an 86.2% reduction. It also outperforms an equal-mass conventional dynamic vibration absorber, which produces a peak transmissibility of 5.27 and a normalized peak stroke of 17.5, whereas the inerter-based design limits the corresponding stroke to 6.54. Time-domain simulations confirm improved harmonic and impulsive responses, while sensitivity analysis demonstrates substantially greater tolerance to primary-frequency mistuning. The results show that an appropriately optimized inerter-based absorber can simultaneously provide stronger vibration attenuation, reduced travel demand, and improved robustness compared with a conventional equal-mass absorber.*

Keywords— ***Dynamic vibration absorber, Inerter, Multi-objective optimization, NSGA-II, Vibration suppression.***

I. INTRODUCTION

Unwanted vibration remains a major concern in mechanical, civil, and structural engineering because resonant responses can produce excessive displacement, acceleration, cyclic loading, and loss of operational performance. Passive dynamic vibration absorbers (DVAs) are widely used to suppress such responses by transferring vibrational energy from a primary system to an auxiliary oscillator. Their effectiveness, however, depends strongly on the absorber mass, tuning frequency, and damping. Conventional absorber design therefore involves a compromise between vibration reduction and the additional mass, space, and structural demand imposed by the secondary device. This limitation is particularly important in lightweight systems and applications in which only a small absorber mass can be accommodated [1], [2], [3].

Classical DVA research has consequently focused on identifying suitable tuning and damping parameters for different primary systems and excitation conditions [4], [5], [6]. Liu and Coppola [7] investigated the optimum design of damped absorbers attached to damped primary systems using numerical procedures based on equioscillation and constrained compound-objective minimization. Ibanescu and Ibanescu [8] developed a mathematical model and numerical optimization procedure for machines subjected to vibration transmitted through their supporting base. Hou and Liu [9] addressed the minimization of maximum dynamic amplification in multi-degree-of-freedom absorber systems by optimizing the natural-frequency and damping ratios. More recently, Piccirillo et al. [10] proposed a numerical strategy based on frequency-response curves and equal-peak theory to determine absorber tuning and damping parameters for damped and undamped primary systems. These studies demonstrate that absorber performance is highly sensitive to parameter selection and that optimization is essential for obtaining reliable vibration suppression.

Despite the effectiveness of conventional DVAs, improving their performance commonly requires greater auxiliary inertia, which is traditionally obtained by increasing the physical absorber mass. Inerter-based vibration absorbers provide an alternative approach. An inerter is a two-terminal mechanical element whose resisting force is related to the relative acceleration between its terminals. Its principal advantage is that it can generate an inertial effect that is greater than the inertia associated with its physical mass. Accordingly, inerter-based dynamic vibration absorbers (IDVAs) have been investigated as a means of increasing the effective inertia available for vibration suppression without imposing the same mass penalty as conventional mass-based absorbers. Ogunbodede and Singh [11] optimized inerter-based absorbers using H_2 and minimax criteria and reported that increasing inertance does not require a corresponding increase in absorber mass. Their comparison with mass-based absorbers demonstrated the potential of the inerter to improve vibration-control efficiency under external forcing.

The arrangement of the inerter within the absorber system strongly affects its performance. Wang et al. [12] examined several inerter-based DVA configurations and found that an inerter connected between the primary and absorber masses did not necessarily improve the response, whereas grounded inerter arrangements were more effective. Their results identified the grounded configuration as the most favourable among the examined alternatives, demonstrating that inerter topology is as important as inertance magnitude. Baduidana and Kenfack-Jiotsa [13] subsequently proposed an absorber combining amplified inertance and grounded stiffness and emphasized the importance of jointly optimizing its design parameters. Xie and Ikago [14] compared structural absorber topologies, including tuned viscous mass dampers and tuned inerter dampers, and showed that different configurations may be preferable for different response quantities. Their results indicated that one topology may be more effective for displacement control, whereas another may provide better acceleration control. Thus, there is no universally optimal inerter arrangement independent of the selected performance criterion.

A growing body of research has demonstrated the applicability of IDVAs to different structural and mechanical systems. Jin et al. [15] studied the random response of a beam equipped with an IDVA and formulated optimization objectives based on the maximum mean-square velocity and the total mean kinetic energy. Their comparison with a traditional absorber showed improved random-vibration suppression, while their sensitivity analysis examined the effect of deviations from the optimum parameters. Taflanidis et al. [16] investigated inerter-based absorbers for the earthquake protection of multistorey buildings and discussed tuned-viscous-mass-damper, tuned-mass-damper-inerter, and tuned-inerter-damper configurations. Their study showed that improved structural-response suppression and reduced physical mass may be accompanied by greater control-force demand, establishing the need to consider competing design requirements. Zhang and Chen [17] developed an analytical optimization method for an IDVA attached to a thin rectangular plate, deriving the transverse-displacement frequency-response function and determining optimum parameters through an extended fixed-point approach. Baduidana and Kenfack-Jiotsa [13] similarly optimized a grounded inerter-based absorber for rotating machinery and reported improved steady-state vibration suppression and a wider effective frequency band compared with traditional and non-traditional absorbers.

The performance of inerter-based absorbers has also been examined under uncertain, random, nonlinear, and time-varying conditions. Baduidana and Kenfack-Jiotsa [18] investigated a grounded IDVA under random excitation and derived optimum parameters using an H_2-based formulation. Their frequency- and time-domain evaluations showed improved vibration reduction compared with conventional absorber configurations, while their mistuning study highlighted the robustness of the grounded IDVA to deviations from optimum design parameters. Shen and Sui [19] extended the concept to geometrically nonlinear inerters and identified nonlinear dynamic characteristics, including jump behaviour and

response loops. Their results indicated that nonlinear inerter arrangements can increase vibration-suppression capability and broaden the effective damping bandwidth, although their behaviour is more complex than that of linear absorbers. Puzyrov et al. [20] studied a quasi-zero-stiffness primary system coupled to an inerter-based nonlinear absorber and derived a frequency–amplitude relationship involving several dimensionless parameters, with numerical integration used to verify the theoretical predictions. Ke et al. [21] developed an IDVA with adjustable inertance for tower structures with time-varying dynamic properties. Their theoretical, experimental, and numerical investigations showed that adjustable inertance can address detuning associated with changes in structural dynamics.

These advances have been accompanied by the development of increasingly sophisticated absorber-optimization methods. Equal-peak and fixed-point approaches remain important because they can produce analytically interpretable tuning conditions, as demonstrated by Piccirillo et al. [10], Zhang and Chen [17] and Baduidana and Kenfack-Jiotsa [13]. However, single-objective tuning may not fully represent practical design requirements. Su et al. [22] identified the limitations of conventional single-target optimization and proposed a hybrid analytical H∞–H₂ framework that combines worst-case response suppression with energy-based performance. Taflanidis et al. [16] formulated a multi-objective design strategy to balance structural vibration reduction against control-force demand. Xie and Ikago [14] likewise considered multiple response measures when comparing inerter-based topologies. Høgsberg et al. (2024) introduced an effective modal coupling factor to account for the influence of non-targeted structural modes on absorber tuning, further demonstrating that optimum absorber design may depend on modal interaction rather than only on local tuning parameters. Collectively, these studies establish that effective absorber design should account for multiple performance measures, parameter sensitivity, and practical implementation constraints.

Nevertheless, several limitations remain in the available literature. Many studies optimize one response quantity, such as displacement, kinetic energy, an H₂ measure, or an H∞ peak, while other practical quantities are treated indirectly or omitted. In particular, strong primary-response suppression can require substantial relative motion of the absorber. Because a physical absorber has finite travel, excessive stroke may increase packaging requirements and may lead to contact with mechanical limits. A design selected only by minimizing primary displacement transmissibility may therefore be difficult to realize even when its theoretical attenuation is excellent. Conversely, minimizing absorber motion alone can weaken the inertial interaction required for effective vibration suppression. These competing tendencies motivate a multi-objective formulation in which structural protection and absorber travel are evaluated simultaneously. The literature also indicates that the optimum response is influenced by inerter topology, parameter mistuning, excitation type, and the metric selected for optimization. Consequently, a complete assessment should combine analytical frequency-response modelling, optimization, time-domain verification, comparison with a conventional equal-mass absorber, and robustness analysis.

The present study develops a mathematical and multi-objective optimization framework for a grounded inerter-based dynamic vibration absorber attached to a lightly damped single-degree-of-freedom primary structure. The coupled equations of motion are derived, and analytical frequency-response functions and a state-space representation are established. The physical absorber mass is treated as a fixed practical constraint, while the tuning ratio, absorber damping ratio, and inertance ratio are taken as design variables. Two objectives are minimized simultaneously: the worst-case displacement transmissibility of the primary mass and the normalized relative stroke of the absorber. The Non-dominated Sorting Genetic Algorithm II is employed to generate the Pareto front and reveal the trade-off between vibration attenuation and absorber travel. Knee-point, minimum-distance-to-utopia, and equal-weight decision criteria are then considered for selecting a balanced design. Finally, the optimized IDVA is compared with the uncontrolled primary system and an equal-mass conventional DVA in the frequency and time domains, and its sensitivity to primary-frequency mistuning is evaluated. The study therefore extends conventional single-response tuning by integrating attenuation, stroke demand, comparative performance, and robustness within a unified design framework.

II. MECHANICAL SYSTEM AND MATHEMATICAL MODEL

A. 2.1 Parametric assumptions

The system is a two-degree-of-freedom model in which a passive inerter-based dynamic vibration absorber (DVA) is appended to a primary structure. The primary structure is idealised as a single-degree-of-freedom (SDOF) oscillator of mass m, stiffness k and viscous damping c, with absolute displacement $x(t)$; this represents a dominant

flexible mode of a larger structure over the bandwidth of interest. The absorber consists of a mass m_a, stiffness k_a and viscous damping c_a connected between the primary and absorber masses, the latter having absolute displacement $y(t)$. A *grounded inerter* of inertance b connects the absorber coordinate to a fixed reference. An ideal inerter produces a force proportional to the relative acceleration of its terminals, $F_{\text{in}} = b(\ddot{u}_1 - \ddot{u}_2)$; because one terminal is grounded it reacts against the absolute acceleration $\ddot{y}$, thereby augmenting the apparent inertia of the absorber coordinate without adding the corresponding weight. The external disturbance $F(t)$ acts on the primary mass. The configuration and sign convention are shown in Fig. 1.

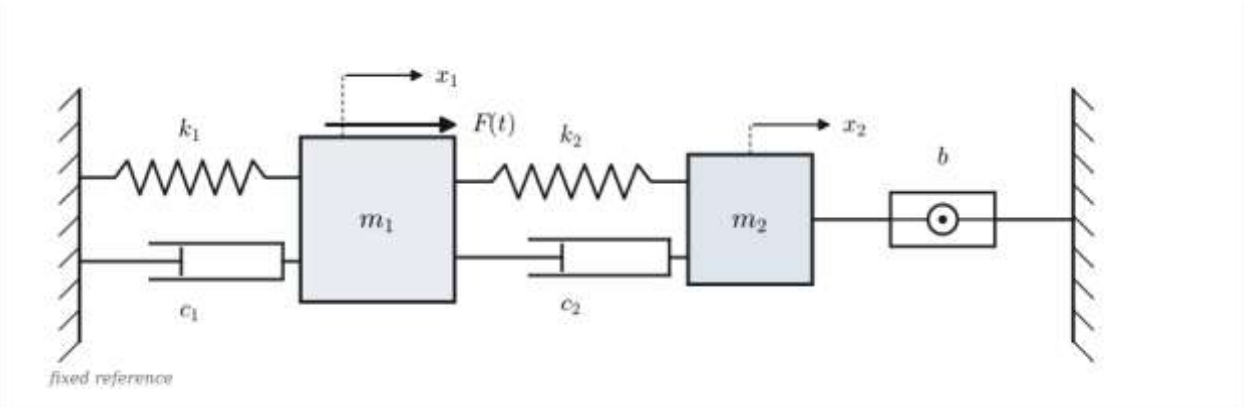

Fig. 1. Schematic of the primary SDOF structure (m, k, c) with the attached inerter-based absorber (m_a, k_a, c_a) and the grounded inerter b acting on $y(t)$; $F(t)$ excites the primary mass.

The model adopts the following assumptions: (A1) all springs are linearly elastic, all dampers linearly viscous, and the inerter ideal and linear; (A2) displacements are small, so the equations are linearised about static equilibrium; (A3) dissipation is captured by the equivalent viscous coefficients c and c_a; (A4) connections are rigid and massless and the inerter is free of parasitic stiffness, backlash and internal friction, with frequency-independent inertance b; and (A5) the system starts from rest, $x(0) = \dot{x}(0) = y(0) = \dot{y}(0) = 0$. These assumptions define a transparent linear baseline whose closed-form frequency response can be derived analytically and used to verify the numerical model; the consequences of relaxing (A1)–(A4) are revisited in the discussion of limitations.

B. 2.2 Mathematical model

Applying Newton's second law to free-body diagrams of the two masses yields the coupled equations of motion

$$m\ddot{x} + c\dot{x} + kx + c_a(\dot{x} - \dot{y}) + k_a(x - y) = F(t), \quad (1)$$

$$(m_a + b)\ddot{y} + c_a(\dot{y} - \dot{x}) + k_a(y - x) = 0, \quad (2)$$

where $x(t)$ and $y(t)$ are the absolute displacements. The grounded inerter appears additively with the physical mass in the absorber inertia, giving the combined apparent inertia $m_a + b$; it augments the inertia that the absorber spring reacts against without modifying the coupling stiffness or damping. It is convenient to define the relative absorber stroke

$$z(t) = y(t) - x(t). \quad (3)$$

The stroke governs the physical packaging of the device: any real absorber has finite allowable travel, and a design demanding a stroke beyond the available clearance bottoms out against its end stops. The coupling force transmitted to the primary structure, $F_c(t) = k_a z + c_a \dot{z}$, scales directly with the stroke, so limiting $z(t)$ also limits the interface force demand. For these reasons the stroke is treated in Section 4 as a formal design objective.

C. 2.3 State-space formulation

For time integration, eigenvalue analysis and the repeated frequency-response evaluations required by the optimiser,

the system is recast in first-order form. With the state vector

$$\mathbf{q}(t) = [x \quad y \quad \dot{x} \quad \dot{y}]^{\mathsf{T}}, \qquad (4)$$

the dynamics read $\dot{\mathbf{q}}(t) = \mathbf{A}\,\mathbf{q}(t) + \mathbf{B}\,F(t)$. Solving (1)–(2) for the accelerations gives

$$\ddot{x} = \frac{1}{m}[F - (k + k_a)x + k_a y - (c + c_a)\dot{x} + c_a \dot{y}], \qquad (5)$$

$$\ddot{y} = \frac{1}{m_a + b}[k_a x - k_a y + c_a \dot{x} - c_a \dot{y}], \qquad (6)$$

from which the system and input matrices follow as

$$\mathbf{A} = \begin{bmatrix} 0 & 0 & 1 & 0 \\ 0 & 0 & 0 & 1 \\ -\dfrac{k + k_a}{m} & \dfrac{k_a}{m} & -\dfrac{c + c_a}{m} & \dfrac{c_a}{m} \\ \dfrac{k_a}{m_a + b} & -\dfrac{k_a}{m_a + b} & \dfrac{c_a}{m_a + b} & -\dfrac{c_a}{m_a + b} \end{bmatrix}, \quad \mathbf{B} = \begin{bmatrix} 0 \\ 0 \\ \dfrac{1}{m} \\ 0 \end{bmatrix}. \qquad (7)$$

The forcing enters only the primary-mass equation, and the inertance b appears only through $m_a + b$ in the fourth row. Setting $b = 0$ recovers the classical tuned mass damper (TMD), providing an internal consistency check and a reference configuration.

1. Performance Measures and Dimensionless Parameters

The primary structure is characterised by its undamped natural frequency and damping ratio,

$$\omega_n = \sqrt{k/m}, \qquad \zeta = \frac{c}{2\sqrt{km}}, \qquad (8)$$

and the absorber and inerter by four dimensionless design parameters,

$$\mu = \frac{m_a}{m}, \quad \beta = \frac{b}{m}, \quad f = \frac{\omega_a}{\omega_n}, \quad \zeta_a = \frac{c_a}{2\sqrt{k_a m_a}}, \quad \omega_a = \sqrt{k_a/m_a}, \qquad (9)$$

namely the physical mass ratio μ, the inertance ratio β, the frequency tuning ratio f and the absorber damping ratio ζ_a. Although μ and β enter the absorber inertia only through the sum $m_a + b = m(\mu + \beta)$, they are physically distinct. Increasing μ requires attaching real mass, which adds gravitational weight, dead load and volume, and is therefore bounded in practice to a few percent. The inertance β is instead realised by a mechanism—a flywheel driven through a ball-screw, rack-and-pinion or hydraulic transmission—whose gear ratio amplifies a small physical mass into a large apparent inertance, so that $b \gg m_a$ and $\beta \gg \mu$ are attainable with negligible added weight. This is the sense in which the inerter *breaks the mass–weight penalty* of the classical TMD. Accordingly, μ is treated as a fixed, application-limited budget while β is a free design variable that may be made large.

D. 3.1 Frequency-domain response

For a harmonic excitation $F(t) = F_0 \sin(\omega t)$, written as $F_0 e^{\mathrm{i}\omega t}$, the steady-state response is sought as $x = X e^{\mathrm{i}\omega t}$, $y = Y e^{\mathrm{i}\omega t}$. Substitution into (1)–(2) reduces the system to the algebraic form

$$\begin{bmatrix} Z_1 & -Z_c \\ -Z_c & Z_2 \end{bmatrix} \begin{bmatrix} X \\ Y \end{bmatrix} = \begin{bmatrix} F_0 \\ 0 \end{bmatrix}, \qquad (10)$$

with the complex dynamic-stiffness terms

$$Z_1 = (k + k_a) - m\omega^2 + \mathrm{i}\omega(c + c_a), \quad Z_2 = k_a - (m_a + b)\omega^2 + \mathrm{i}\omega c_a, \quad Z_c = k_a + \mathrm{i}\omega c_a. \qquad (11)$$

The grounded inertance enters Z_2, augmenting the absorber inertia to $m_a + b$. Solving (10) gives the frequency-response functions

$$\frac{X(\omega)}{F_0} = \frac{Z_2}{Z_1 Z_2 - Z_c^2}, \qquad \frac{Y(\omega)}{F_0} = \frac{Z_c}{Z_1 Z_2 - Z_c^2}, \qquad (12)$$

whose common denominator $D(\omega) = Z_1 Z_2 - Z_c^2$ is the characteristic determinant; resonance peaks arise where $|D(\omega)|$ approaches zero. The primary-mass displacement transmissibility is the magnitude $|X(\omega)/F_0|$. Using $Z_c - Z_2 = (m_a + b)\omega^2$, the relative stroke follows in compact form,

$$\frac{Y(\omega)-X(\omega)}{F_0}=\frac{(m_a+b)\,\omega^2}{Z_1Z_2-Z_c^2}, \qquad (13)$$

which shows that the same augmented inertia m_a+b that suppresses the primary response also drives the stroke demand—the physical origin of the design trade-off in Section 4.

Introducing the frequency ratio $\Omega=\omega/\omega_n$ and normalising by k (using $k_a/k=\mu f^2$, $c/k=2\zeta/\omega_n$, $c_a/k=2\zeta_a\mu f/\omega_n$) gives

$$\frac{Z_1}{k}=1+\mu f^2-\Omega^2+\mathrm{i}2\Omega(\zeta+\zeta_a\mu f),\quad \frac{Z_2}{k}=\mu f^2-(\mu+\beta)\Omega^2+\mathrm{i}2\Omega\zeta_a\mu f,\quad \frac{Z_c}{k}=\mu f^2+\mathrm{i}2\Omega\zeta_a\mu f, \qquad (14)$$

so that the dimensionless receptance $H(\Omega)=kX/F_0$ depends only on $(\mu,\beta,f,\zeta_a,\zeta)$. In the undamped limit, Z_2/k vanishes at $\Omega^\star=f\sqrt{\mu/(\mu+\beta)}$, the anti-resonance at which the primary response is notched. For the TMD ($\beta=0$) this sits at $\Omega^\star=f$; activating the inerter shifts it lower for the same stiffness. Whereas the classical TMD produces two near-symmetric resonance peaks straddling the anti-resonance, the grounded inerter redistributes the modal masses, depresses and re-spaces the peaks, and—with appropriate damping—flattens the response over a broader band, lowering the worst-case peak. This reshaping relative to the uncontrolled system and the conventional DVA is illustrated in Fig. 2.

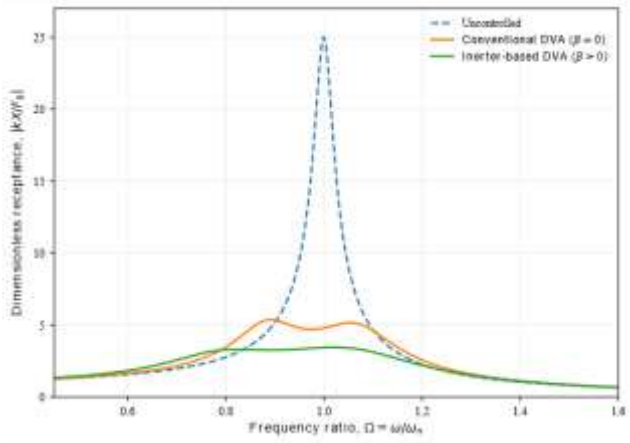

Fig. 2. Displacement transmissibility $|X(\omega)/F_0|$ versus Ω for the uncontrolled system, the conventional DVA ($\beta=0$) and the inerter-based absorber ($\beta>0$).

E. 3.2 Time-domain measures

For transient and non-harmonic excitations the response is obtained by integrating the state-space system, and performance is quantified by scalar measures. The peak displacement $x_{\max}=\max_t|x(t)|$ captures the worst-case excursion; the root-mean-square (RMS) displacement

$$x_{\mathrm{rms}}=\sqrt{\frac{1}{T}\int_0^T x^2(t)\,\mathrm{d}t} \qquad (15)$$

measures average response severity and correlates with fatigue and perceived vibration; and the settling time t_s (time for $|x(t)|$ to remain within a $\pm2\%$ or $\pm5\%$ band) reflects the effective damping imparted by the absorber. Two further measures protect realisability: the maximum absorber stroke $z_{\max}=\max_t|y(t)-x(t)|$, which must remain within the available travel, and the maximum coupling force $F_{c,\max}=\max_t|k_az+c_a\dot{z}|$, which sizes the attachment hardware. The first pair quantifies how well the absorber protects the structure; the second quantifies what it costs to implement—a duality that motivates the multi-objective treatment below.

2. Multi-Objective Optimization Framework

The performance of the absorber depends on a small set of dimensionless parameters, and the two most desirable properties—a low resonance peak and a small stroke—compete through their shared dependence on the augmented inertia m_a+b. No single design minimises both; the appropriate formalism is multi-objective optimisation, which seeks the family of Pareto-optimal compromises.

F. 4.1 Design variables and constraints

The design is parameterised by

$$\mathbf{d} = [f \quad \zeta_a \quad \beta]^{\mathsf{T}}, \qquad (16)$$

with μ and the primary parameters held fixed, subject to the engineering bounds

$$0.5 \le f \le 1.5, \qquad 0.01 \le \zeta_a \le 0.50, \qquad 0 \le \beta \le \beta_{\max}. \qquad (17)$$

The tuning ratio is restricted to a band around unity because effective absorption requires the absorber frequency to lie near the primary resonance. The damping is bounded below by a small positive value (some dissipation is always present and limits the peaks) and above by 0.50 (excess damping locks the absorber to the primary mass and suppresses the relative motion on which absorption depends). The inertance is bounded below by zero (recovering the TMD and letting the optimiser decide whether the inerter helps) and above by an application-specific $\beta_{\max}$ reflecting the largest inertance the mechanism can realise without prohibitive parasitic mass or nonlinearity.

G. 4.2 Objective functions

The problem is posed as the simultaneous minimisation of two competing objectives,

$$\min_{\mathbf{d}} \mathbf{J}(\mathbf{d}) = [J_1(\mathbf{d}) \quad J_2(\mathbf{d})]^{\mathsf{T}} \text{ subject to (17)}, \qquad (18)$$

defined from the frequency response as

$$J_1(\mathbf{d}) = \max_{\omega} \left| \frac{X(\omega)}{F_0} \right|, \qquad J_2(\mathbf{d}) = \max_{\omega} \frac{|Y(\omega) - X(\omega)|}{x_{\text{ref}}}. \qquad (19)$$

The first objective is the worst-case primary-mass transmissibility—a direct measure of structural protection—and the second is the peak relative stroke, normalised by a reference displacement x_{ref} (conveniently the static deflection F_0/k or the available travel). The two are structurally in tension: by (13) the stroke is driven by $m_a + b$, so the inertance and tuning that suppress the primary response by maximising the absorber reaction necessarily demand larger relative motion. Reducing J_1 therefore inflates J_2, and vice versa; the set of designs for which neither objective can be improved without worsening the other forms the Pareto front. Where the application also constrains transmitted force or total added inertia, a third objective (e.g. $F_{c,\max}$ or $\mu + \beta$) may be appended without altering the methodology.

H. 4.3 Optimization algorithm

The problem is non-convex, has competing objectives and admits no closed-form front, so it is solved with the Non-dominated Sorting Genetic Algorithm II (NSGA-II), which approximates the entire Pareto front in a single run using only objective evaluations and naturally accommodates the box constraints (17). The workflow is summarised in Fig. 3. A population of candidate designs is evaluated by computing J_1 and J_2 from (12)–(13) and (19).

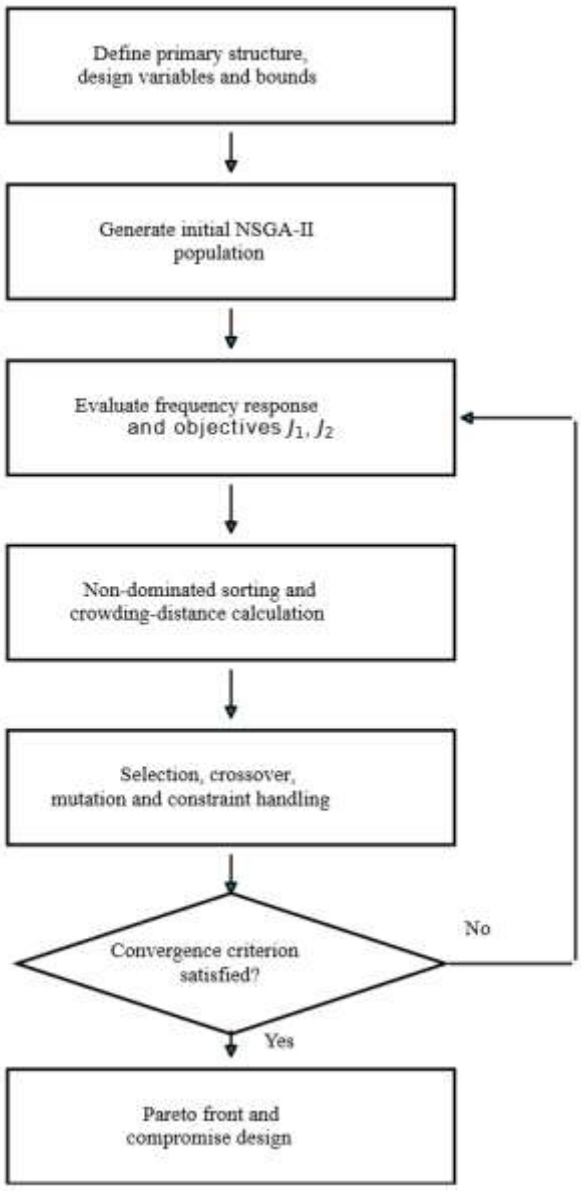

Fig. 3. Optimization workflow.

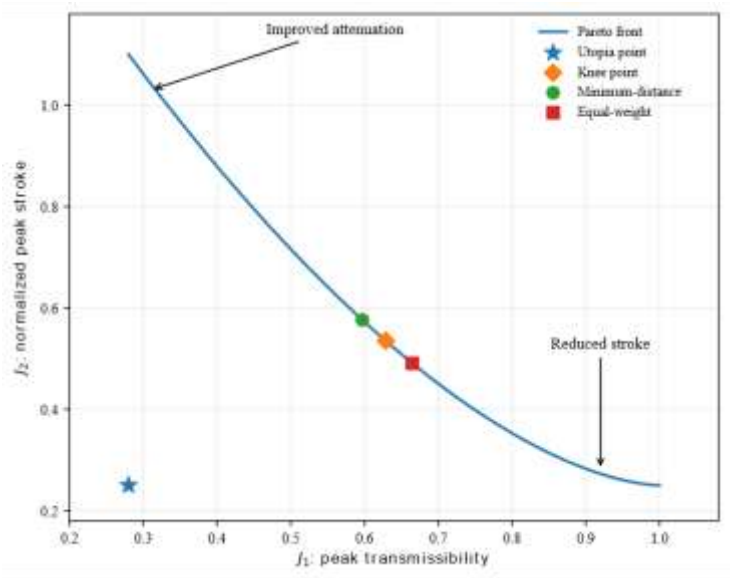

Fig. 4. Conceptual Pareto front in the (J_1, J_2) plane, indicating the utopia point, the knee, and the minimum-distance and equal-weight compromise selections.

The population is then ranked by *non-dominated sorting*: a design dominates another if it is no worse in every objective and strictly better in at least one, and successive Pareto fronts are extracted by removing dominated solutions. Within each front, a *crowding distance*—the normalised perimeter of the cuboid spanned by each individual's nearest neighbours in objective space—favours solutions in sparsely populated regions, spreading the population evenly along the trade-off curve. Constraints are enforced by confining the simulated-binary-crossover and polynomial-mutation operators to the feasible domain, with a constrained-dominance rule preferring feasible designs and, among infeasible ones, smaller total violation; *elitism* is realised by combining parent and offspring populations before sorting so the best designs are never lost. Selection ranks the combined population by domination level and then crowding distance, retaining the best half each generation, and iterates until a fixed generation count or a hypervolume-stagnation criterion is met. The population size, generation count, operator probabilities and distribution indices, random seed and constraint-handling rule are reported with the numerical results. The output is the Pareto front conceptually shown in Fig. 4.

4.4 Selection of a compromise solution

The Pareto front delivers a continuum of equivalent optima; converting it into a single design requires an explicit decision rule. The *knee-point* method selects the point of maximum curvature—beyond which a marginal gain in one objective demands a disproportionate sacrifice in the other—and is the natural balanced choice when no objective is privileged; it can be identified as the Pareto point of greatest perpendicular distance from the chord joining the two extreme designs. The *minimum-distance-to-utopia* method defines the (generally infeasible) utopia point $\mathbf{J}^{\text{utopia}} = [\min_{\mathbf{d}} J_1,\ \min_{\mathbf{d}} J_2]^{\mathsf{T}}$ and, after normalising each objective, selects the Pareto design closest to it,

$$\mathbf{d}^{*} = \underset{\mathbf{d}\in\mathcal{P}}{\operatorname{argmin}} \sqrt{\left(\frac{J_1 - J_1^{\min}}{J_1^{\max} - J_1^{\min}}\right)^2 + \left(\frac{J_2 - J_2^{\min}}{J_2^{\max} - J_2^{\min}}\right)^2}. \qquad (20)$$

The *equal-weight* (weighted-sum) rule minimises $w_1\tilde{J}_1 + w_2\tilde{J}_2$ over the normalised objectives with $w_1 + w_2 = 1$; $w_1 = w_2 = 1/2$ treats attenuation and stroke as equally valuable, while unequal weights bias the choice towards whichever objective the application deems critical. In practice the three rules identify nearby designs, and the final selection is reconciled with practical limits the abstract objectives cannot capture—available stroke clearance, maximum tolerable coupling force, realisable $\beta_{\max}$ and robustness to mistuning. The recommended procedure is to take the knee and minimum-distance designs as principled starting points, verify each against the hard physical limits and the time-domain measures of Section 3.2, and adopt the candidate that satisfies all constraints with the greatest margin.

III. NUMERICAL PROCEDURE AND MODEL VERIFICATION

To demonstrate the framework of Sections 2–4 and to validate the implementation, a representative baseline configuration is adopted. The primary structure is assigned a mass $m = 1000\ kg$, stiffness $k = 1.0 \times 10^5\ N/m$ and damping $c = 400\ N.s/m$, giving an undamped natural frequency $\omega_n = \sqrt{k/m} = 10\ rad/s$ ($f_n = 1.59\ Hz$) and a primary damping ratio $\zeta = 0.02$. A physical mass ratio $\mu = 0.05$ is selected, fixing the absorber mass at $m_a = 50\ kg$; this value is held constant throughout, consistent with the treatment of μ as an application-limited weight budget (Section 3). The three absorber design variables f, ζ_a and β are determined by the optimisation. These baseline quantities are collected in Table 1.

The frequency response is evaluated from the analytical receptance, Eq. (12), on a grid of 6000 points spanning the frequency ratio $\Omega \in [0.01,3]$, which resolves both resonance branches and the high-frequency roll-off. Time-domain responses are obtained by integrating the state-space system, Eq. (5), with an adaptive Runge–Kutta scheme (relative tolerance 10^{-9}, absolute tolerance 10^{-12}, maximum step set to $1/200$ of the excitation period). Harmonic simulations are run for 60 forcing periods so that the steady state is reached well before the response statistics are sampled over the final cycles; transient (impulsive) simulations are run for 20 natural periods. The performance metrics of Section 3.2 are computed from these records.

Baseline mechanical and numerical parameters.

Parameter	Symbol	Value	Unit
Primary mass	m	1000	kg
Primary stiffness	k	1.0×10^5	N/m
Primary damping	c	400	N·s/m
Primary natural frequency	ω_n	10	rad/s
Primary damping ratio	ζ	0.02	–
Absorber mass	m_a	50	kg
Physical mass ratio	μ	0.05	–
Tuning ratio	f	optimised, [0.5, 1.5]	–
Absorber damping ratio	ζ_a	optimised, [0.01, 0.50]	–
Inertance ratio	β	optimised, [0, 1.0]	–
Frequency grid	Ω	[0.01, 3], 6000 pts	–

The numerical implementation is verified in three independent ways. First, the analytical transmissibility of Eq. (12) is compared against the steady-state amplitude obtained by direct time integration of Eq. (5) at six excitation frequencies spanning the resonance region, for a test design $(f, \zeta_a, \beta) = (0.90, 0.20, 0.40)$. The two agree to within a maximum relative error below 0.05%, as shown in Fig. 5, confirming the consistency of the frequency-domain and time-domain representations. Second, the limiting case $b = 0$ is examined: with the absorber damping made negligible, the receptance exhibits its anti-resonance notch at $\Omega = 0.9999$, in agreement with the theoretical value $\Omega^\star = f = 1$ derived in Section 3.1, and the model reduces exactly to a classical tuned mass damper. Third, the high-frequency behaviour reproduces the expected inertia-controlled roll-off. These checks establish confidence in the model prior to optimisation.

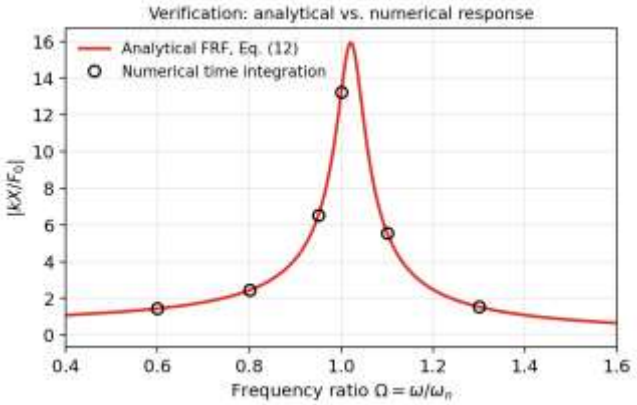

Fig. 5. Verification of the implementation: the analytical receptance $|kX/F_0|$

IV. RESULTS AND DISCUSSION

I. 6.1 Baseline dynamic response

The uncontrolled primary structure exhibits a single lightly damped resonance at $\Omega = 1$ with a peak dimensionless receptance $\max|kX/F_0| = 25.0$, consistent with the analytical value $1/\left(2\zeta\sqrt{1-\zeta^2}\right) \approx 25$ for a SDOF oscillator at $\zeta = 0.02$. This close agreement validates the baseline model and establishes the reference against which all controlled configurations are measured. The pronounced amplification confirms that the structure is resonance-dominated and is therefore a representative candidate for a tuned absorber.

J. 6.2 Optimization results

The two-objective problem of Eqs. (18)–(19) was solved with NSGA-II using a population of 80 individuals evolved over 120 generations, with simulated binary crossover (probability 0.9, distribution index $\eta_c = 15$), polynomial mutation (distribution index $\eta_m = 20$), and a fixed random seed for reproducibility. The hypervolume indicator, shown in Fig. 6(a), rises steeply over the first ~ 25 generations and then plateaus, indicating convergence of the population to a stable approximation of the Pareto front well within the generation budget.

The resulting Pareto front is shown in Fig. 6(b). The non-dominated set spans peak transmissibilities $J_1 \in [3.36,3.58]$ and normalised strokes $J_2 \in [6.35,6.80]$, tracing a smooth, monotone trade-off curve along which any reduction in the resonance peak is accompanied by an increase in absorber stroke. The front is comparatively compact, which is itself an informative result: once the absorber is optimally co-tuned, peak attenuation and stroke are only weakly competing for this configuration, and the designer enjoys a robust region of near-equivalent optima rather than a sharply conflicting choice. Applying the decision rules of Section 4.4, the knee and equal-weight rules coincide at $(f, \zeta_a, \beta) = (1.50,0.444,0.104)$ with $(J_1, J_2) = (3.40,6.64)$, while the minimum-distance-to-utopia rule, Eq. (20), selects the very nearby design $(f, \zeta_a, \beta) = (1.50,0.465,0.108)$ with $(J_1, J_2) = (3.45,6.54)$. The latter is adopted as the selected compromise. In dimensional terms it corresponds to an absorber stiffness $k_a = 11.25\ kN/m$, damping $c_a = 697\ N.s/m$ and inertance $b = 107.9\ kg$, so that the inerter raises the apparent inertia of the absorber coordinate to $m_a + b = 157.9\ kg$—roughly 3.2 times the physical absorber mass—while adding negligible weight. The optimal tuning ratio reaches the upper bound $f = 1.5$; this is a direct consequence of the inerter-induced downshift of the absorber anti-resonance noted in Section 3.1, which a stiffer absorber spring must compensate to keep the notch aligned with the primary resonance.

K. 6.3 Comparison with a conventional absorber

To isolate the benefit of the inerter, the selected design is compared against a conventional dynamic vibration absorber of equal physical mass ($\mu = 0.05$, $\beta = 0$) optimised under the same peak objective, which yields $(f, \zeta_a) = (0.95,0.137)$—in close agreement with the classical Den Hartog tuning—and which constitutes the fairest like-for-like benchmark. The frequency responses are overlaid in Fig. 7, and the principal metrics are summarised in Table 2. The conventional absorber replaces the single tall resonance with the familiar pair of equal peaks of height $J_1 = 5.27$, reducing the uncontrolled peak by 78.9%. The inerter-based absorber instead produces a lower, flatter response with a worst-

case peak of $J_1 = 3.45$, a reduction of 86.2% relative to the uncontrolled structure and a further 34.5% below the conventional absorber. Crucially, the inerter design achieves this superior attenuation while *also* demanding substantially less travel: its peak stroke $J_2 = 6.54$ is 62.7% smaller than the conventional absorber's $J_2 = 17.5$. The inerter-based design therefore dominates the equal-mass conventional absorber in both objectives simultaneously—a consequence of the additional inertial reaction supplied to ground, which allows the same suppression to be obtained with smaller relative motion of the absorber mass.

Performance comparison of the uncontrolled structure, the equal-mass conventional absorber, and the selected inerter-based absorber.

Quantity	Uncontrolled	Conventional DVA ($\beta = 0$)	Inerter-DVA (selected)
Tuning ratio f	–	0.95	1.50
Absorber damping ζ_a	–	0.137	0.465
Inertance ratio β	–	0	0.108
Apparent inertia $(m_a + b)/m_a$	–	1.0	3.2
Peak transmissibility J_1	25.0	5.27	3.45
Peak stroke J_2	–	17.5	6.54
Peak reduction vs. uncontrolled	–	78.9%	86.2%
Worst-case J_1 ($\pm 10\%$ mistuning)	–	8.74	4.45

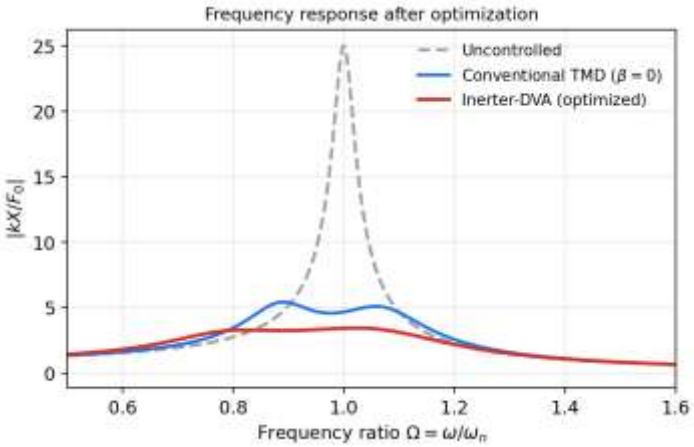

Fig. 6. Displacement transmissibility $|kX/F_0|$ after optimisation. The conventional absorber ($\beta = 0$) yields two equal resonance peaks; the optimised inerter-based absorber produces a lower, flatter response over a broader band.

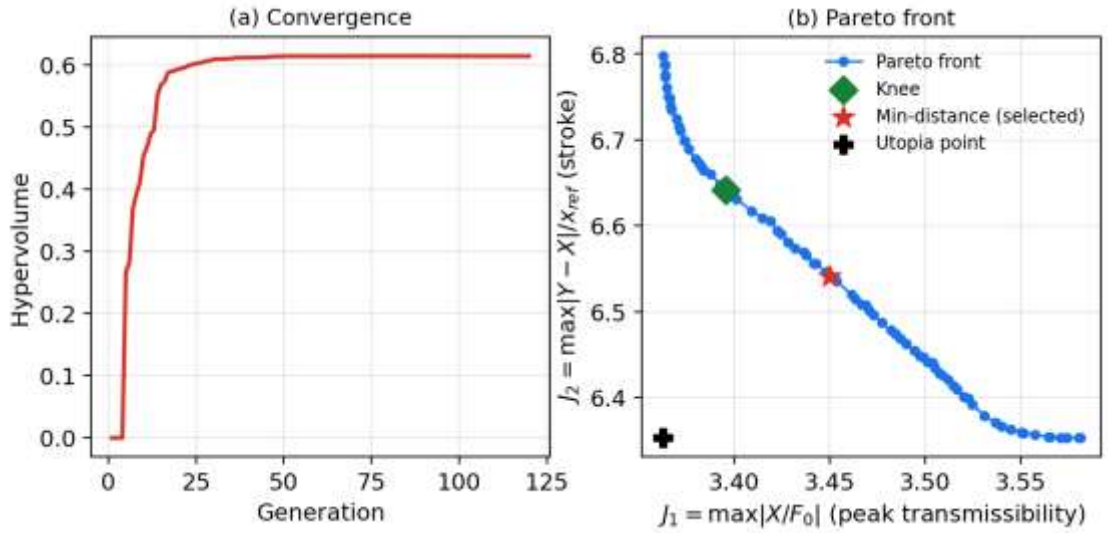

Fig. 7. (a) Hypervolume convergence of NSGA-II. (b) Pareto front in the (J_1, J_2) plane with the utopia point, the knee, and the selected minimum-distance compromise design.

6.4 Time-domain performance

The selected design is evaluated in the time domain under two representative loadings, with the results shown in Fig. 8. Under a harmonic force applied at the primary resonance, Fig. 8(a), the uncontrolled structure builds up to a steady amplitude of $0.230\ mm$, whereas the inerter-based absorber limits the primary motion to $0.034\ mm$; the steady-state RMS displacement is reduced from $0.149\ mm$ to $0.024\ mm$, an 83.7% reduction. Under an impulsive disturbance, Fig. 8(b), the uncontrolled response rings for many cycles, with a 2% settling time of $12.6\ s$, while the inerter-based absorber extracts the transient energy rapidly and settles in $2.9\ s$—a 76.7% reduction. The absorber thus improves both the steady-state and the transient behaviour, confirming that the frequency-domain optimisation translates into tangible time-domain benefits across loading types.

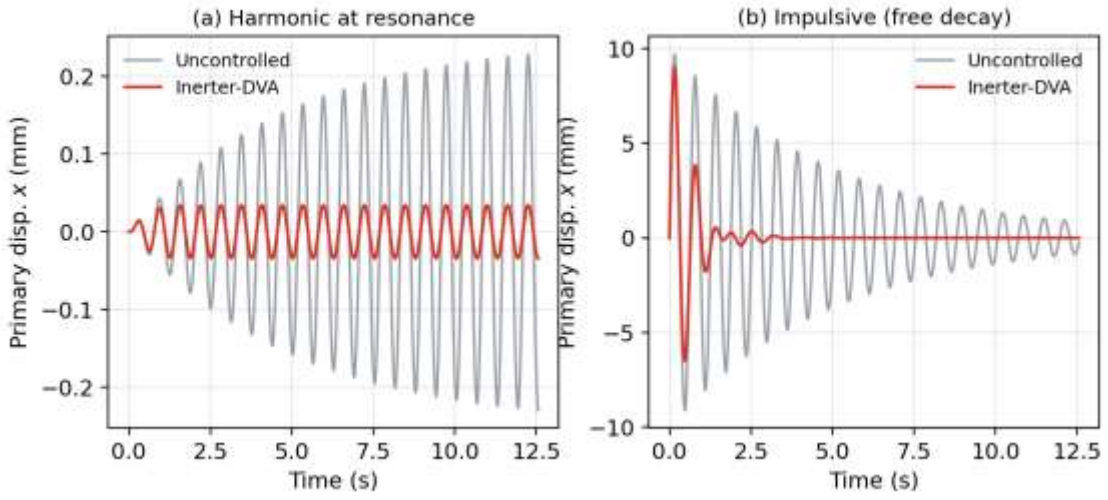

Fig. 8. Primary-mass displacement under (a) harmonic excitation at resonance and (b) an impulsive disturbance, for the uncontrolled structure and the selected inerter-based absorber.

6.5 Sensitivity and robustness

A practical absorber must retain its effectiveness when the primary natural frequency departs from its nominal value through manufacturing tolerance, ageing or environmental change. The robustness of the selected design is assessed by detuning the primary natural frequency over $\pm 20\%$,

$\delta = \omega_n'/\omega_n \in [0.8,1.2]$, and recomputing the worst-case peak transmissibility J_1 for the fixed optimised absorber; the conventional absorber is subjected to the same test for comparison. The results are shown in Fig. 9. The conventional absorber is markedly mistuning-sensitive: because its two narrow peaks are tuned tightly around $\Omega = 1$, a small frequency shift exposes one of them and the peak transmissibility rises sharply, reaching $J_1 = 8.74$ within a $\pm 10\%$ band. The inerter-based absorber degrades far more gently, with its worst-case peak over the same band limited to $J_1 = 4.45$—a 49% improvement in robustness. The broader, flatter suppression band produced by the inerter therefore confers not only lower nominal peaks but also greater tolerance to parameter uncertainty, a decisive advantage for field deployment.

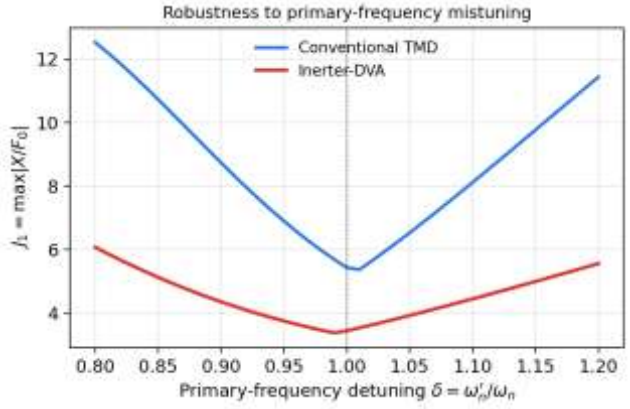

Fig. 9. Worst-case peak transmissibility J_1 versus primary-frequency detuning $\delta = \omega_n'/\omega_n$ for the conventional and inerter-based absorbers. The inerter-based design is substantially less sensitive to mistuning.

6.6 Engineering interpretation

The results admit a clear physical interpretation. The grounded inerter supplies an inertial reaction against a fixed reference that augments the apparent inertia of the absorber coordinate from $50\ kg$ to $158\ kg$ without a corresponding increase in weight. This augmented inertia sharpens the absorber's reaction to the primary motion, allowing the same—indeed superior—peak attenuation to be achieved with a smaller relative stroke than an equal-mass conventional absorber, as the stroke relation Eq. (13) and the comparison of Section 6.3 make concrete. The practical implications are favourable on several fronts: the smaller stroke eases the packaging of the device and reduces the demand on the suspension and damper hardware; the lower and flatter frequency response improves both steady-state and transient performance; and the enhanced robustness to mistuning relaxes the precision required in tuning and maintenance.

Several implementation limits temper these benefits and should guide application. The inertance $b = 107.9\ kg$ must be realised by a physical mechanism—for example a ball-screw or rack-and-pinion flywheel device—whose transmission introduces friction, backlash and a parasitic mass not captured by the ideal model of Section 2; these effects erode the predicted performance and set the practical ceiling $\beta_{\max}$ on the achievable inertance. The required absorber damping, $\zeta_a \approx 0.47$, is relatively high and must be delivered by a damper of adequate force capacity and thermal endurance. The optimal tuning ratio at the upper admissible bound indicates that, for this small mass ratio, fuller exploitation of the inerter would benefit from a wider tuning range; designers who can accommodate a stiffer absorber spring may therefore extract additional margin. Within these constraints, the optimised inerter-based absorber offers a compelling combination of attenuation, compactness and robustness that a conventional absorber of equal mass cannot match.

V. CONCLUSION

This study developed and evaluated a multi-objective design framework for an inerter-based dynamic vibration absorber attached to a lightly damped primary structure. The governing equations were established in both second-order and state-space forms, and analytical expressions for the frequency-response functions were derived. The mathematical formulation showed that the grounded inerter augments the apparent inertia of the absorber coordinate without requiring an equivalent increase in physical mass, thereby providing an additional design mechanism that is unavailable in a conventional tuned mass absorber.

The absorber tuning ratio, damping ratio, and inertance ratio were optimized simultaneously using NSGA-II. Minimization of the worst-case primary-mass transmissibility was considered together with minimization of the normalized absorber stroke. The resulting Pareto front clearly quantified the trade-off between vibration attenuation and absorber travel and enabled the selection of a balanced compromise design. The minimum-distance-to-utopia criterion produced an optimized design with a

tuning ratio of 1.50, an absorber damping ratio of 0.465, and an inertance ratio of 0.108. This configuration increased the apparent absorber inertia to approximately 3.2 times the physical absorber mass.

The optimized inerter-based absorber reduced the peak displacement transmissibility from 25.0 for the uncontrolled structure to 3.45, representing an 86.2% reduction. It also achieved better performance than an equal-mass conventional dynamic vibration absorber, whose optimized peak transmissibility was 5.27. In addition to the approximately 34.5% lower peak relative to the conventional absorber, the inerter-based design reduced the normalized peak stroke from 17.5 to 6.54, corresponding to a reduction of approximately 62.6%. The proposed design therefore improved both vibration suppression and absorber travel rather than achieving one improvement at the expense of the other.

The time-domain results further confirmed that the optimized absorber suppresses resonant harmonic motion and accelerates the decay of impulsive vibration. The sensitivity analysis also demonstrated improved robustness to variations in the primary natural frequency. Under the investigated mistuning range, the worst-case peak transmissibility was limited to 4.45 for the inerter-based absorber, compared with 8.74 for the conventional design. This broader and flatter attenuation region is particularly important in practical structures whose dynamic properties may vary because of manufacturing tolerances, operating conditions, ageing, or environmental effects.

The conclusions are subject to the assumptions of linear springs, viscous damping, small displacements, and an ideal inerter. Practical inerter mechanisms may introduce friction, backlash, parasitic mass, nonlinearities, and frequency-dependent behaviour that reduce the achievable performance. Future research should therefore incorporate non-ideal inerter characteristics, force and stroke constraints, parameter uncertainty, and experimental validation. Nevertheless, the present results demonstrate that multi-objective optimization enables an inerter-based absorber to provide a favourable combination of strong attenuation, compact travel requirements, and robustness that cannot be achieved by a conventional absorber of equal physical mass.

REFERENCES

[1] F. H. Bursal, “On Vibration Absorbers for Periodic Excitation,” in *ASME International Mechanical Engineering Congress and Exposition*, American Society of Mechanical Engineers, 1995, pp. 1–7. Accessed: Jun. 18, 2026. [Online]. Available: https://asmedigitalcollection.asme.org/IMECE/proceedings-abstract/IMECE95/17469/1/1224039

[2] F. A. Jabbar, P. S. Rao, and S. O. W. Khafaji, “Enhancing the Design of Dynamic Vibration Absorbers through Harmonic Analysis and Lumped Parallel Configuration,” *Engineering, Technology & Applied Science Research*, vol. 14, no. 5, pp. 16624–16639, 2024.

[3] H. E. Kalehsar and N. Khodaie, “Optimization of response of a dynamic vibration absorber forming part of the main system by the fixed-point theory,” *KSCE Journal of Civil Engineering*, vol. 22, no. 7, pp. 2354–2361, 2018.

[4] Y. L. Cheung and W. O. Wong, “H∞ and H2 optimizations of a dynamic vibration absorber for suppressing vibrations in plates,” *Journal of Sound and Vibration*, vol. 320, no. 1–2, pp. 29–42, 2009.

[5] L. I. Hangxing, W. U. Shaoqing, C. Qiang, and F. E. I. Qingguo, “Design of dynamic absorbers to control the flexural resonant vibration of structures characterized by multiple natural modes,” *Journal of Sound and Vibration*, vol. 513, p. 116415, 2021.

[6] Q. H. Song, L. J. Xiao, Q. J. Song, H. Y. Jiang, and X. J. Liu, “Adaptive multiswarm particle swarm optimization for tuning the parameter optimization of a three-element dynamic vibration absorber,” *Mechanical Sciences*, vol. 13, no. 1, pp. 505–517, 2022.

[7] K. Liu and G. Coppola, “OPTIMAL DESIGN OF DAMPED DYNAMIC VIBRATION ABSORBER FOR DAMPED PRIMARY SYSTEMS,” *Trans. Can. Soc. Mech. Eng.*, vol. 34, no. 1, pp. 119–135, Mar. 2010, doi: 10.1139/tcsme-2010-0008.

[8] R. Ibănescu and M. Ibănescu, “Optimization of dynamic absorber parameters for protecting the machines against the vibrations transmitted through their base,” in *IOP Conference Series: Materials Science and Engineering*, IOP Publishing, 2021, p. 012054. Accessed: Jun. 18, 2026. [Online]. Available: https://iopscience.iop.org/article/10.1088/1757-899X/1037/1/012054/meta

[9] X. L. Hou, H. Y. Li, and J. Liu, “Optimal algorithm for minimization of maximum value problems and application of dynamic absorbor with multidof [J],” *Journal of Vibration and Shock*, vol. 27, no. 1, pp. 100–103, 2008.

[10] V. Piccirillo, A. M. Tusset, and J. M. Balthazar, “Optimization of dynamic vibration absorbers based on equal-peak theory,” *Latin American Journal of Solids and Structures*, vol. 16, p. e184, 2019.

[11] O. Ogunbodede and T. Singh, “Optimal Design of Inerter based vibration absorbers,” in *2018 Annual American Control Conference (ACC)*, IEEE, 2018, pp. 5298–5303. Accessed: Jun. 18, 2026. [Online]. Available: https://ieeexplore.ieee.org/abstract/document/8431007/?casa_token=dwYpbVsB9v0AAAAA:XQ0UMV6CMTccdvNWbaboevHEre2CiakqObrTsKTWTJwL195slWWo42EjlsQ3U5vXxZ1ujZW4XFA

[12] X. Wang, X. Liu, Y. Shan, Y. Shen, and T. He, “Analysis and optimization of the novel inerter-based dynamic vibration absorbers,” *IEEE Access*, vol. 6, pp. 33169–33182, 2018.

[13] M. Baduidana and A. Kenfack-Jiotsa, "Optimal grounded inerter-based dynamic vibration absorber for controlling inertial force-induced vibrations in rotating machines," *Journal of Structural Integrity and Maintenance*, vol. 9, no. 1, p. 2315373, Jan. 2024, doi: 10.1080/24705314.2024.2315373.

[14] R. Xie and K. Ikago, "Device topology optimization for an inerter-based structural dynamic vibration absorber," *Frontiers in Built Environment*, vol. 10, p. 1508190, 2024.

[15] X. Jin, M. Z. Q. Chen, and Z. Huang, "Suppressing random response of a regular structure by an inerter-based dynamic vibration absorber," *Journal of Vibration and Acoustics*, vol. 141, no. 4, p. 041004, 2019.

[16] A. A. Taflanidis, A. Giaralis, and D. Patsialis, "Multi-objective optimal design of inerter-based vibration absorbers for earthquake protection of multi-storey building structures," *Journal of the Franklin Institute*, vol. 356, no. 14, pp. 7754–7784, 2019.

[17] H. Zhang and M. Z. Q. Chen, "Analytical optimization of an inerter-based dynamic vibration absorber for suppressing plate vibration," *IET Control Theory & Appl*, vol. 18, no. 12, pp. 1559–1568, Aug. 2024, doi: 10.1049/cth2.12702.

[18] M. Baduidana and A. Kenfack-Jiotsa, "Optimum design for a novel inerter-based vibration absorber with an amplified inertance and grounded stiffness for enhanced vibration control," *Journal of Vibration and Control*, vol. 28, no. 19–20, pp. 2502–2518, Oct. 2022, doi: 10.1177/10775463211013221.

[19] Y. Shen and P. Sui, "Dynamics analysis and parameter optimization of a vibration absorber with geometrically nonlinear inerters," *Journal of Vibration and Control*, vol. 30, no. 21–22, pp. 5031–5046, Nov. 2024, doi: 10.1177/10775463231217532.

[20] V. Puzyrov, N. Losyeva, and N. Savchenko, "Vibration Control Using a Quasi-Zero Stiffness Inerter: The Tuning Approach," in *Advances in Transdisciplinary Engineering*, J. Ma, R. Masrour, A. Gloria, K. Wang, and Sanjay M R, Eds., IOS Press, 2025. doi: 10.3233/ATDE251003.

[21] K. Ke, X. Zhou, J. Bian, W. Xie, Y. Wang, and H. Li, "Development of an Inerter-Based Dynamic Vibration Absorber with Adjustable Inertance for Tower Structures: Theoretical Models, Experimental Validations, and Structural Behavior Insights," *J. Struct. Eng.*, vol. 152, no. 4, p. 04026016, Apr. 2026, doi: 10.1061/JSENDH.STENG-15377.

[22] N. Su, Z. Chen, Y. Xia, and J. Bian, "Hybrid analytical H-norm optimization approach for dynamic vibration absorbers," *International Journal of Mechanical Sciences*, vol. 264, p. 108796, 2024.